

## Simulation and Experimental Validation of Flow-Current Characteristic of a Sample Hydraulic Servo Valve

M.S. Sadooghi<sup>1,\*</sup>, R. Seifi<sup>1</sup> and M. Saadat Foumani<sup>2</sup>

**Abstract.** *This paper presents a novel model to simulate the flow-current characteristic curve of an electro-hydraulic servo valve in steady state condition. This characteristic curve has three major zones: dead zone, linear zone and saturation zone. By using the presented approach, we can simulate the behavior of all types of valves including under lapped, critical center (zero lapped) and over lapped valves. A hydraulic tester has been designed and constructed for validation of the results. It can test the performance of flow-current and some other properties of the valve. Comparison of experimental and simulated curves describes that the model has an acceptable accuracy in determining the four important valve characteristics: flow gain, saturation flow, saturation current and dead zone. As a result, the model can be used for other studies such as geometrical sensitivity analysis (the ultimate objective of this modeling) or design optimization. Since this model is presented in a computer based algorithm, it can be easily used to observe and measure the effects of change in the parameters of interest (particularly geometrical parameters of the valve) on the flow-current curve.*

**Keywords:** *Hydraulic servo valve; Torque motor; Pilot circuit; Spool; Flow-current curve.*

### INTRODUCTION

Electro-hydraulic systems, as one of the major parts of power production and transmission systems, are widely used in various industries. The main advantages of these systems are high power-to-weight ratio, ability to produce and transmit very high power and inherent self-cooling [1]. Control valves are the main part of control process in these systems. These valves are usually employed in two forms: servo and proportional. The manufacturing precisions distinguish proportional valves from servo valves [2]. Their differences principally can be revealed in the lapping between spool and ports. If this lapping is more than 3% of port diameter, it is a proportional valve and if it is less than 3% of port diameter, it is a servo valve [3]. Overlapped spool in proportional valves leads to less sensitivity to the oil

pollutions, but on the other hand causes a dead zone characteristic in the flow gain. Under lapped spool or critical center (zero lapped) in servo valves leads to higher response but may increase the instability (in the vicinity of equilibrium position of spool) due to the increasing flow gain [2]. Servo and proportional valves are modeled for various purposes which can be design optimization, linear and nonlinear controller design and sensitivity analysis.

In the last decades, some researchers have published some works in the field of servo valves modeling. These papers usually have been founded on derivation of governing dynamic and fluid equations of the valve operation. Linearization of these equations leads to a transfer function between input and output variables. In one of the significant works, Merritt [4] presented a third-order model. Tawfic [1] presented a sixth-order model for the first stage of a servo valve with a feedback spring by using dynamic and fluid analysis and aids from Merritt's works. Transfer function input is the current and the output is the spool position. The valve was assumed in the critical center mode. Mokherejee modeled a servo hydraulic valve with a force motor [5]. He studied the sensitivity of flow-current curves to some geometrical characteristics the

1. *Department of Mechanical Engineering, School of Engineering, Bu-Ali Sina University, Hamedan, P.O. Box 65175-4161, Iran.*

2. *School of Mechanical Engineering, Sharif University of Technology, Tehran, P.O. Box 11155-9567, Iran.*

\*. *Corresponding author. E-mail: ms.sadooghi@alum.sharif.edu*

*Received 17 September 2009; received in revised form 12 June 2010; accepted 14 August 2010*

valve in the steady state condition. Kim and Tsao [6] presented a fifth-order equation for modeling the first stage of a servo valve with a feedback spring. Noah [7] presented a linearized model for output flow of the valve. He studied the geometrical effects of the ports for optimization of linear operation of the valves. Also he derived governing dynamic equations of flapper in a two stage nozzle-flapper valve. Eryilmaz and Wilson [2] derived a nonlinear continuous model with the aid of orifice equation for the second stage of the valve for all types of lapping. Amirante et al. [8] calculated the fluid forces on the spool of an underlapped hydraulic directional valve by Computational Fluid Dynamics (CFD). Also Del Vescovo and Lippolis [9] used CFD method for determination of fluid forces on spool.

In overall, it seems that there is no comprehensive servo valve model that represents all parts of the valve and can simulate both first and second stages simultaneously. In this work, a sample servo valve without feedback spring is modeled to obtain a simulation of steady state flow-current behavior of the valve. Because of the effects of the geometrical details in sensitivity analysis, we are interested in these details. At first, torque motor and pilot circuit (first stage) of the valve are modeled. Then, the CFD method was used for the modeling of the second stage. Finally, by combination of the first and second stage models of the valve, flow-current characteristic curve is obtained. This simulated curve has been compared with experimental curve obtained from the hydraulic tester.

**MODELING**

A schematic view of servo valve components is shown in Figure 1. Magnetic solenoid which is actuated by

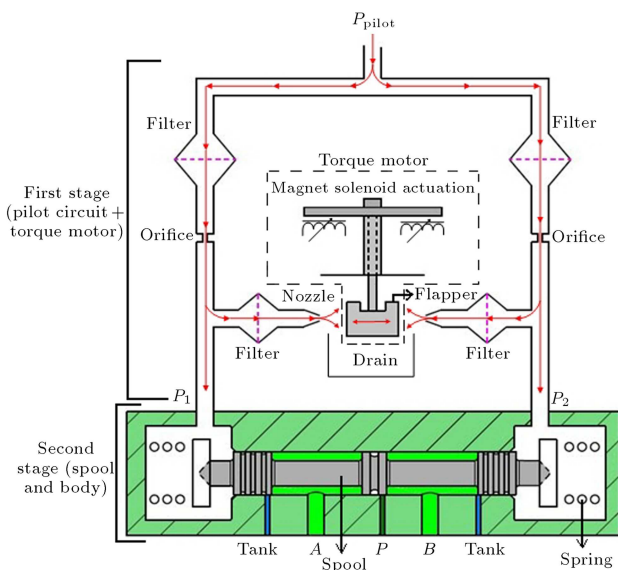


Figure 1. A schematic view of the valve.

input electrical current inclines the flapper towards one of the nozzles. In this situation, the symmetry of pilot circuit is disturbed and the flow rate in the near nozzle becomes less than the far nozzle. It causes a pressure difference ( $\Delta p$ ) between two sides of the spool. Spool displacement is proportional to this  $\Delta p$ . Port opening value is a function of the spool displacement. By this mechanism, ports can be controlled electrically with high accuracy. For instance if the spool moves to the left in Figure 1, the high pressure hydraulic fluid flows from port “P” to port “B” (load line) via spool body space. Also low pressure hydraulic fluid flows from port “A” to storage tank at the same time. In the next sections, simulation of this mechanism by modeling and analysis of the behaviors of all components is presented.

**Torque Motor Modeling**

Actually, torque motor is a part of the first stage or amplifier stage, but as it is the only electro-mechanical part of the valve, it was modeled separately. The aim of the modeling is derivation of an equation for determination of the applied forces by motor to the armature. An attractive-repulsive torque motor type has been used in this sample valve. A schematic view of the torque motor is depicted in Figure 2. Steady magnetic flux is supplied by four permanent magnets that are made of Alnico5. The control coil was constructed by two parallel coils with 2500 turns. Magnetic flux density of the permanent magnets was measured to be 0.3 T. Electromagnetic model of torque motor circuit is presented in Figure 3. According to this model and using Kirchhoff rules, we have:

$$E + Ni = R_1\phi_1 + R_4\phi_4, \tag{1}$$

$$E - Ni = R_3\phi_3 + R_2\phi_2, \tag{2}$$

where  $E$ ,  $N$ ,  $i$ ,  $R$  and  $\phi$  are electrical potential number of turns in the coil, current, reluctance and magnetic flux, respectively. Because of symmetry, we have:

$$\phi_1 = \phi_4, \tag{3}$$

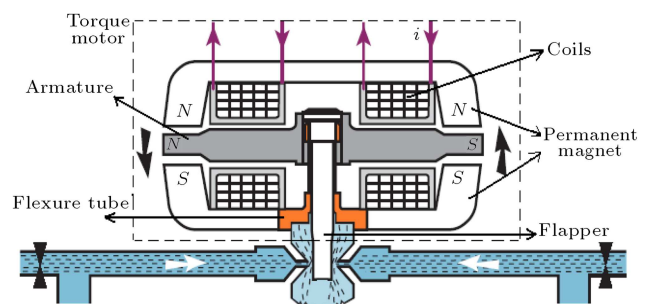


Figure 2. A schematic view of the torque motor .

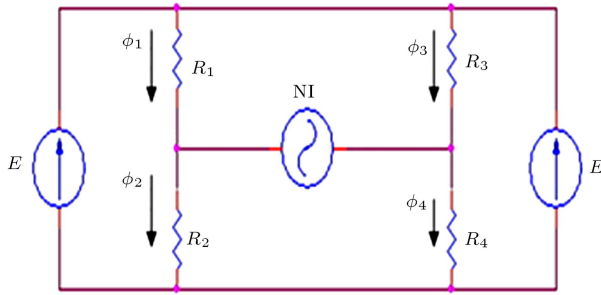


Figure 3. Electromagnetic model of the torque motor.

$$\phi_2 = \phi_3, \tag{4}$$

$$R_1 = R_4, \tag{5}$$

$$R_2 = R_3. \tag{6}$$

The reluctance  $R$  is the summation of air and body reluctances which are the first and second terms of Equations 7 and 8, respectively [10]:

$$R_1 = R_4 = \frac{(k-x)}{\mu_0 A} + \frac{(k-x)}{\mu_0 \mu_r A}, \tag{7}$$

$$R_2 = R_3 = \frac{(k+x)}{\mu_0 A} + \frac{(k+x)}{\mu_0 \mu_r A}, \tag{8}$$

where  $k$  is the equilibrium distance of armature and body,  $x$  is the displacement of the armature end,  $A$  is the area normal to the flux path in the air gap,  $\mu_0$  is the magnetic permeability of air and  $\mu_r$  is the relative magnetic permeability of the substance. Flux relations can be derived with the aid of the Equations 1 to 8 as:

$$\phi_1 = \frac{E + Ni}{\frac{2(k-x)}{\mu_0 A} + \frac{2(k-x)}{\mu_0 \mu_r A}}, \tag{9}$$

$$\phi_2 = \frac{E - Ni}{\frac{2(k+x)}{\mu_0 A} + \frac{2(k+x)}{\mu_0 \mu_r A}}. \tag{10}$$

A coefficient of 2 appears in the denominators of Equations 9 and 10 because of the existence of two air gaps and two magnetic body sections above and below the armature. So the magnetic flux density is obtained as:

$$B_1 = \phi_1/A \rightarrow B_1 = \frac{(E + Ni)\mu_0 \mu_r}{2(\mu_r k - \mu_r x + k - x)}, \tag{11}$$

$$B_2 = \phi_2/A \rightarrow B_2 = \frac{(E - Ni)\mu_0 \mu_r}{2(\mu_r k + \mu_r x + k + x)}. \tag{12}$$

To derive an equation for the applied magnetic forces on the armature, at first, energy in the gap between the armature and the body is calculated. Then by differentiating the energy equation with respect to the armature displacement ( $x$ ), an expression is

derived to calculate the force. Equations 13 and 14 represent foregoing energy in attraction and repulsion conditions [10]:

$$w_1 = \frac{B_1^2(A(k-x))}{\mu_0}, \quad (\text{Attraction}) \tag{13}$$

$$w_2 = \frac{B_2^2(A(k+x))}{\mu_0}. \quad (\text{Repulsion}) \tag{14}$$

The forces are obtained by means of differentiation:

$$f_1 = -\frac{\partial w_1}{\partial x}, \tag{15}$$

$$f_2 = -\frac{\partial w_2}{\partial x}. \tag{16}$$

According to Figure 4, these two forces can be seen as a couple that is applied on the armature. The summation of  $f_1$  and  $f_2$  can be calculated as:

$$f = f_1 + f_2 = \frac{-A\mu_r^2\mu_0[ENik^2 + kN^2i^2x + kE^2x + ENix^2]}{(\mu_r k + \mu_r x + k + x)^2(k-x)^2}. \tag{17}$$

### Armature-Flapper Modeling

Armature-flapper set is a medium between the torque motor and the pilot circuit. It transmits the produced torque from motor to the pilot circuit. Main parts of this set are armature, flapper and flexure tube.

### Armature-Flapper Dynamics

Figure 5 shows a free body diagram of the armature and flapper assembly. Referring to this figure and using the

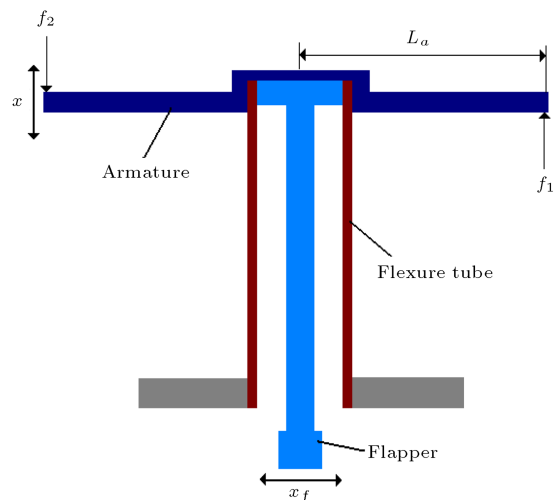
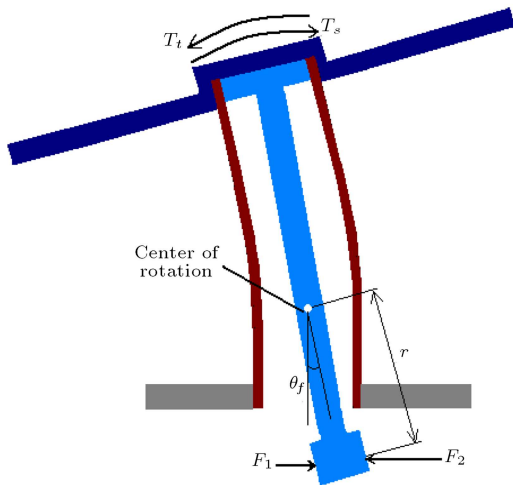


Figure 4. A simple model of the flapper, armature and flexure tube.



**Figure 5.** Free body diagram of the flapper, armature and flexure tube.

torque balance, the governing dynamic equation of the armature and flapper can be expressed as:

$$T_t - T_s - (F_1 - F_2)r = J\ddot{\theta} + c\dot{\theta}, \quad (18)$$

where  $T_t$  is the generated torque by the torque motor,  $T_s$  is the resistance torque of the flexure tube,  $F$  is the pilot fluid force,  $r$  is the radius of the flapper from the pivot to the pilot fluid forces,  $J$  is the polar mass moment of inertia of the flapper and the armature,  $c$  is the damping coefficient of the armature and the flapper and  $\theta_f$  is the rotation angle of the flapper. Since the sample valve is studied in steady state condition, the dynamic effects due to the motion of the armature-flapper mechanism are not considered in this work. Indeed, in each step, the output flow of the valve or other quantities have been modeled or measured in the state which input current has a constant value. This implies that the right side of Equation 18 equals zero. So it can be said that the steady state equation of the armature-flapper is:

$$T_t - T_s - (F_1 - F_2)r = 0. \quad (19)$$

According to Figure 5 and by use of Equation 17,  $T_t$  can be written as:

$$T_t = \frac{A\mu_r^2\mu_0[iENk^2 + i^2kN^2x + kE^2x + iENx^2]}{(\mu_rk + \mu_rx + k + x)^2(k - x)^2} L_a, \quad (20)$$

where  $L_a$  is the arm length of the armature. In the flexure tube it can be assumed that  $T_s = K_s\theta_f$  where  $K_s$  is the stiffness of the flexure tube. Also  $r = \frac{x_f}{\theta_f}$  and  $L_a = \frac{x}{\theta_f}$  [1] ( $x_f$  is the flapper displacement). Equation 20 was validated by an experiment. In this test  $T_t$  was measured as a function of input current when  $\theta_f$  and  $x_f$  are fixed on zero ( $x_f = \theta_f = 0$ ) by applying extra input current to the torque motor. The

armature and the flapper are considered as a rigid set. According to Figure 5, if  $\theta_f = 0$  then  $x = x_f = 0$ . This constraint omits the effects of the flexure tube stiffness for this specimen. The comparison of experimental and theoretical data (obtained from Equation 20 with  $x = x_f = 0$ ) is shown in Figure 6. As can be seen, the calculated values from Equation 20 have an acceptable accuracy.

**Flexure Tube Stiffness**

The stiffness of the flexure tube was obtained by an experimental procedure. As it is shown in Figure 7, the torque motor is separated from the valve set. Displacement of the flapper ( $x_f$ ) versus the input current was measured in the absence of hydraulic fluid. In Figure 8 the results of this experiment are shown. After some algebraic calculations,  $T_t$  versus  $\theta_f$  was obtained and plotted in Figure 9. The slope of the

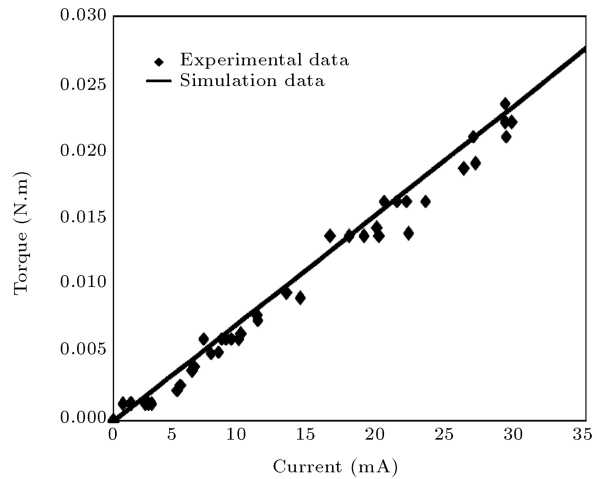


**Figure 6.** Comparison of the simulated torque with the experimental torque as functions of the input current when  $x_f = \theta_f = 0$ .

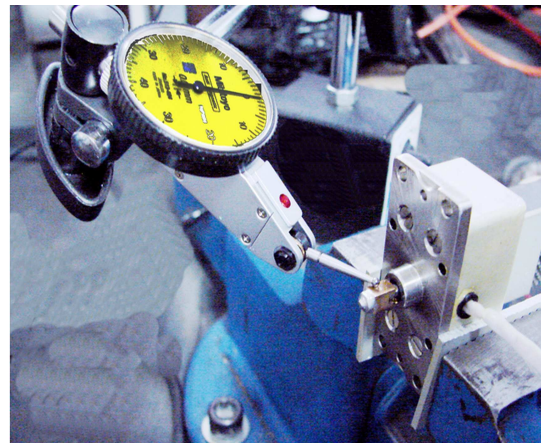


**Figure 7.** Measuring the flapper displacement in terms of the input current (torque motor is separated from the valve set).

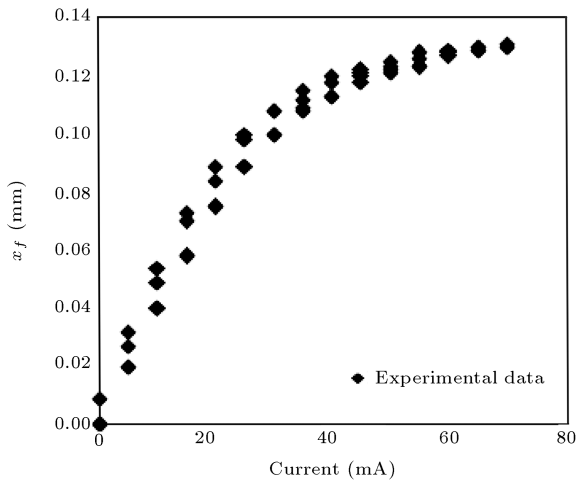


Figure 8. Flapper displacement versus input current (in the absence of pilot fluid forces).

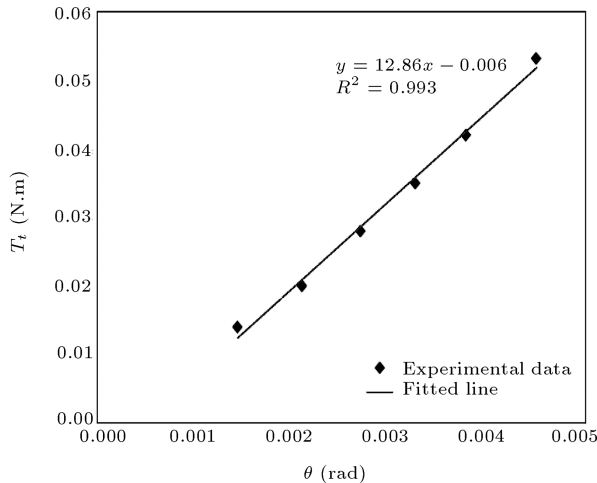


Figure 9. Stiffness of the flexure tube.

fitted line is the stiffness of the flexure tube. In this test, this value was found to be 12.86 N.m/rad.

### FLUID ANALYSIS OF PILOT CIRCUIT

#### Fluid Forces

According to Figure 10, all of the applied forces on the flapper due to the hydraulic fluid of the pilot circuit can be listed as follow [11]:

- Pressure exerted force ( $F_P$ ) is the major force:

$$F_P = \frac{\pi}{4} d_n^2 p_n K_q \quad (21)$$

- Momentum exerted force ( $F_M$ ) which is presented by:

$$F_M = 8\pi(C_d(L + x_f))^2 p_n k_q \quad (22)$$

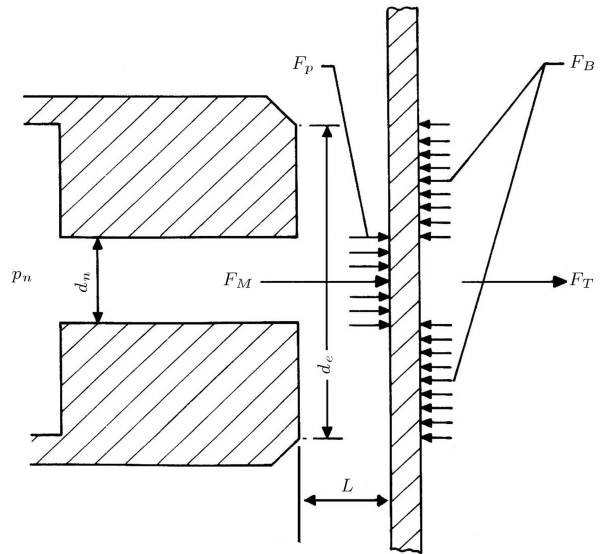


Figure 10. Fluid forces on the flapper.

- Bernoulli force ( $F_B$ ) which is:

$$F_B = \pi(C_d d_n)^2 \left\{ \ln \left( \frac{d_e}{d_n} \right) - \frac{1}{2} \left[ 1 - \left( \frac{d_n}{d_e} \right)^2 \right] \right\} p_n K_s \quad (23)$$

In these equations  $k_q$  is obtained from:

$$k_q \cong \frac{1}{1 + 16 \left( L + \frac{x_f}{d_n} \right)^2} \quad (24)$$

Finally, the resultant force that is applied to the flapper from each nozzle is calculated as:

$$F_T = F_P + F_M - F_B \quad (25)$$

However, as can be seen in Figure 5, the exerted fluid forces on that flapper side which is nearer to the nozzle, are larger than the opposite forces ( $F_2 > F_1$ ). The calculated resultant force on the flapper is presented in Figure 11.

#### Flow- Pressure Relations

As shown in Figure 1, the hydraulic fluid in the pilot circuit flows into some major elements such as filter, orifice and the nozzle. As a result, there is some pressure drop due to these elements as well as the friction in pipes (channels). Also it is known that the total supply pressure of the hydraulic fluid at the pilot circuit is 45 bar (4500 KPa) and the pressure on the drain is 7 bar (700 KPa). Therefore, there is 38 bar pressure drop across the pilot circuit. Also the flow rate within the nozzle-flapper distance

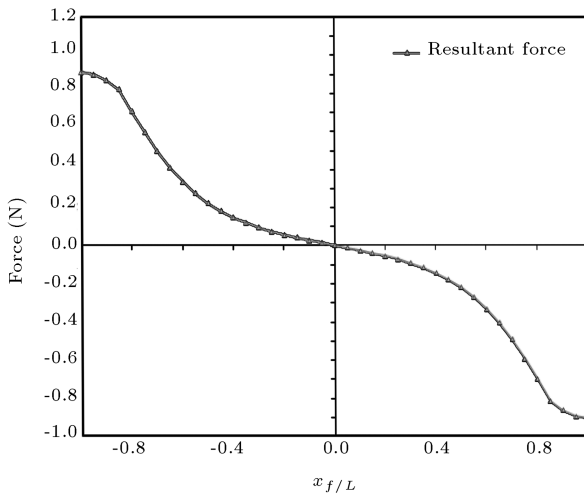


Figure 11. Resultant fluid force versus  $x_f/L$ .

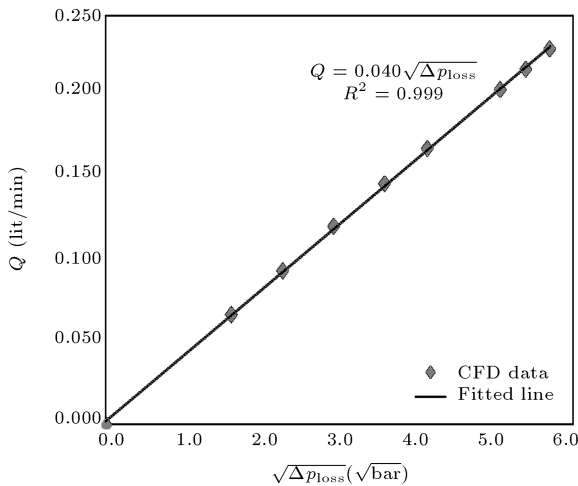


Figure 12. Flow values versus  $\sqrt{\Delta p}$  in the orifice.

must be known. The relations between the flow and  $\sqrt{\Delta p}$  in the orifice, nozzle-flapper and the filters were calculated by CFD method. It was revealed that the pressure drops in the filters and channels are negligible, compared to the orifice and the nozzle-flapper. In Figure 12, the variations of the flow versus  $\sqrt{\Delta p}$  is presented for the orifice. The figure was obtained from simulating an axisymmetric model with CFD method. The fluid flow was assumed to be turbulent, and  $K-\epsilon$  model was used. Input and output pressures were applied as boundary conditions. In the case of the nozzle-flapper, it is obvious that the distance between these two elements varies during the valve operation. Since the equilibrium distance is 0.06 mm for this sample valve, the flow- $\sqrt{\Delta p}$  curve was plotted for few points in vicinity of this equilibrium distance. The required data in other internal distances are obtained by interpolation. These curves are shown in Figure 13. Details of the model are similar to the foregoing model of orifice.

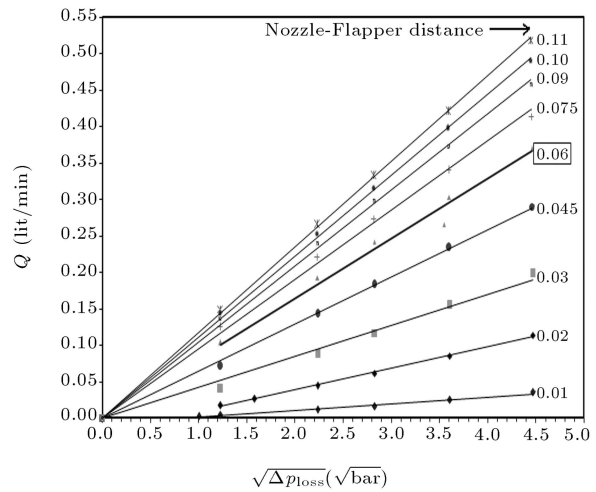


Figure 13. Flow values versus  $\sqrt{\Delta p}$  in various distances of the flapper and nozzle.

## SIMULATION

### Equilibrium Angle of Flapper

As it was explained in previous sections, the flapper displacement in terms of the input current was obtained by experiment (in the absence of the pilot hydraulic fluid). However, in a real situation there is hydraulic pilot fluid that flows from the nozzles to the flapper. When the flapper tilts towards each of the nozzles, a hydraulic force is exerted to the flapper in the opposite direction, so its equilibrium angle is reduced. For calculation of this new angle, the following two steps should be done:

1. For initial guess, by means of Figure 8, the flapper angle is calculated in terms of the input current in the absence of the fluid forces by using  $x_f = r\theta_f$ .
2. The calculated angle is then used for calculation of the components of Equation 19. If we set this equation as:

$$G = T_t - T_s - (F_1 - F_2)r,$$

by trial and error, the  $\theta_f$  is found for  $G(\theta_f) = 0$ . If  $G(\theta_f) > 0$ , then we reduce  $\theta_f$  and vice versa. This process should be continued to find the desired angle ( $\theta_f$ ). According to Figure 5 and  $x_f = r\theta_f$  the  $x_f$  is derived too.

### Spool Displacement

As it is seen in Figures 12 and 13, the pressure drop in the orifice and nozzle can be written as:

$$\Delta p_{\text{orifice}} = C_1 Q', \tag{26}$$

$$\Delta p_{\text{nozzle}} = C_2(x_f)Q', \tag{27}$$

where  $Q' = Q^2$ ,  $C_1$  is a constant and  $C_2(x_f)$  is a function of  $x_f$  ( $x_f$  was derived previously so  $C_2(x_f)$  can be derived from Figure 13). According to Figure 1, it is clear that the flow rate of the nozzle and orifice in each side of the pilot circuit is equal. Also it was mentioned that the total pressure in the pilot circuit is 45 bar and the drain pressure is 7 bar. By neglecting the pressure drops in the filters and pipes it can be said that the whole pressure drop occurs in the orifice and the nozzle-flapper throats. As a result, one can say:

$$\Delta p_{\text{orifice}} + \Delta p_{\text{nozzle}} = \Delta p_{\text{total}} = 38. \quad (28)$$

From Equations 26 to 28,  $Q'$  can be written as:

$$Q' = \frac{\Delta p_{\text{total}}}{C_1 + C_2(x_f)} = \frac{38}{C_1 + C_2(x_f)}. \quad (29)$$

This process should be done for each side of the pilot circuit and a distinct flow rate is obtained for each nozzle. Now, it can be claimed that the pressures in the downstream of the two orifices have been determined. In Figure 1 it is clear that the pressure behind each side of the spool is equal to downstream pressure of corresponding orifice. Multiplying pressure difference to the section area of the spool yields the resultant applied force to the spool in steady state condition. Since the stiffness of the spool spring is known, the displacement can be calculated. The lapping phenomena can be then considered simply in this stage where the “port opening” ( $P_o$ ) is related to the spool displacement by:

$$P_o = S_d - l_p \begin{cases} l_p > 0 & \text{overlapped} \\ l_p = 0 & \text{critically} \\ l_p < 0 & \text{underlapped} \end{cases} \quad (30)$$

where  $P_o$  is the port opening,  $S_d$  is the spool displacement and  $l_p$  is the lapping of the spool and port. If  $P_o < 0$ , the port has not opened yet. In the studied valve,  $0.005 \text{ mm} < l_p < 0.01 \text{ mm}$ .

All processes in this section are simulated using a computer based algorithm where the input is the current and the output is the control port opening. The spool displacement versus the input current is shown in Figure 14.

**Output Flow**

As it is seen in Figure 15, the spool displacement controls the output flow of the valve. In fact, the spool and the ports (machined on the spool body) are used as a variable orifice. In Figure 1, it is obvious that the displacement of the spool is controlled by the pressure difference between two sides of the spool which is due to the flapper movement between the two nozzles.

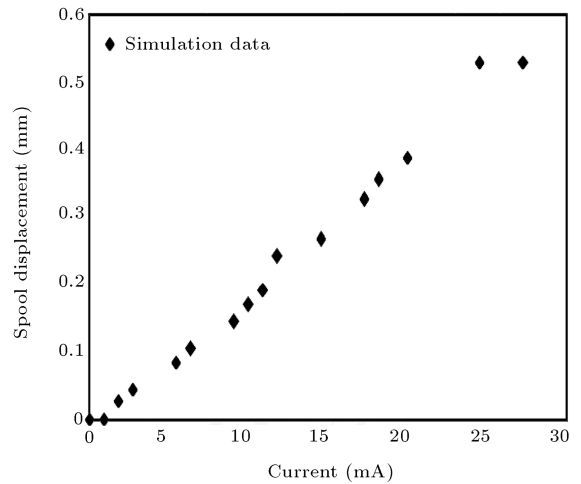


**Figure 14.** Spool displacement versus the input current.

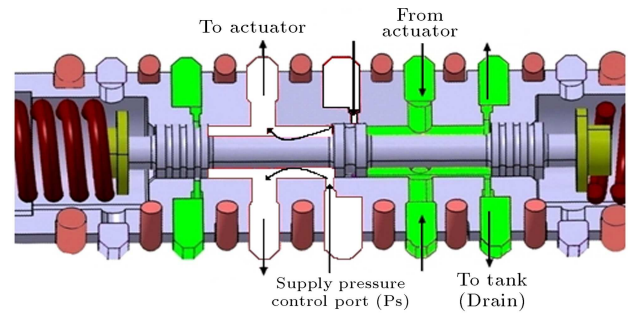


**Figure 15.** Section of the spool body and ports (spool has moved to the right from its equilibrium position).

According to Figures 1 and 15, this sample valve has two types of ports. One is the control port (such as ports  $P$  and Tank in Figure 1) that is used as a variable orifice and its opening is proportional to the spool movement. The other type is used to direct the flow towards the actuator or from it (such as ports  $A$  and  $B$  in Figure 1). These ports are not controlled proportionally. Therefore, for modeling of the spool and ports, by paying attention to Figures 1 and 15, a model such as the one shown in Figure 16 is proposed. Also in this figure, boundary conditions which are used in CFD modeling are shown. The model is axisymmetric. Pressure boundary conditions were

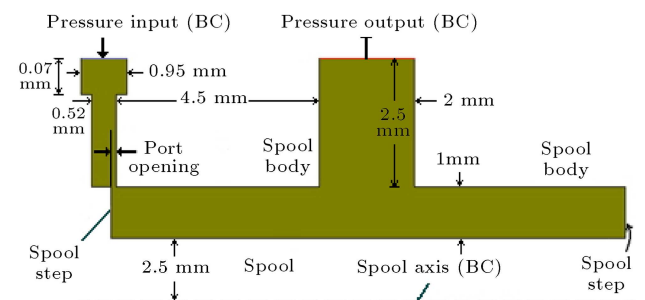


**Figure 16.** The CFD model of the spool body and the ports along with the related Boundary Conditions (BC).

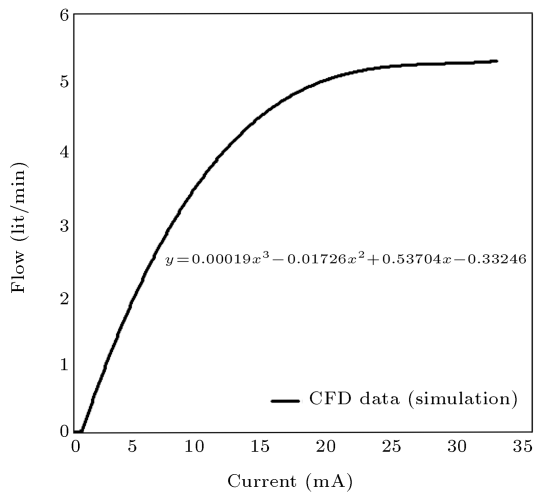


**Figure 17.** Simulated flow-current curve (dead zone, linear zone and saturation zone are seen).

applied and output flow rate was obtained. Fluid flow was assumed turbulent and  $K-\Omega$  model was used for solving. This model was solved for various opening of the control port. Since the relation between the port opening and the input current was presented in Figure 14, the curve of the flow rate versus current is obtained in steady state condition. The recent curve is the main objective of this work. This graph is shown in Figure 17. The simulation is performed in a nominal supply pressure of 100 bar.

### Summary of Simulation

- Flapper displacement is derived from Figure 8 for an arbitrary input current (0-35 mA).  $\theta_f = \frac{x_f}{r}$  is the initial guess for the angle which is used for solving Equation 19.
- Equation 19 was then solved by trial and error ( $T_t$  was obtained from Equation 20,  $T_s$  is obtained from  $T_s = K_s \theta_f$  and ' $F_1 - F_2$ ' is derived from Figure 11).
- The flow rate of the nozzle and orifice is derived by means of three algebraic Equations 26 to 28 in each side of the pilot circuit.
- The downstream pressure difference of two orifices was calculated. It is the same pressure difference of the two sides of the spool (Figure 1). With the aid of spool spring stiffness, spool displacement versus input current was obtained (Figure 14).
- Output flow is obtained by CFD method as discussed previously and shown in Figure 17.

### EXPERIMENTAL RESULTS AND MODEL VALIDATION

For obtaining experimental data, a hydraulic tester was designed according to the SAE-ARP490 Rev E

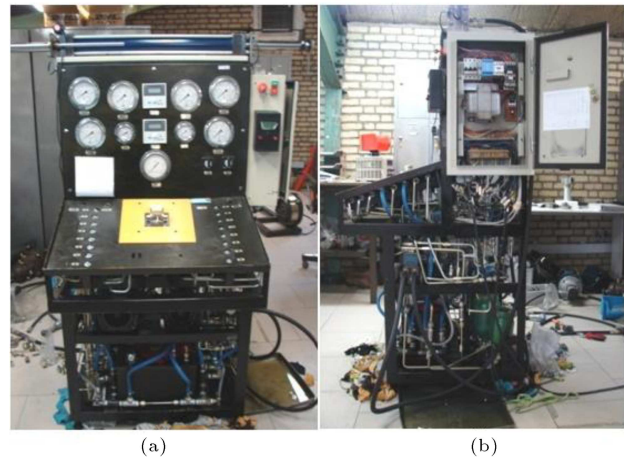


**Figure 18.** (a) Front view of the hydraulic tester. (b) Side view of the hydraulic tester.

standard. In Figures 18a and 18b, two views of this hydraulic tester are seen. For flow measurement, a hydraulic jack and an encoder are used that is seen in Figure 18a. This jack can provide loading and unloading conditions. In this work, all tests were in unloading and steady state conditions. In order to provide pilot and load (supply) flow, two distinct pumps are used. The sample valve is set up on the tester and receives input current between 0 to 35 mA in 50 steps. The time of a complete course of the jack is measured. Then with the aid of cylinder dimensions (course: 90 cm and input diameter: 5 cm) and some calculations, the corresponding flow rate for each input current can be obtained. The pilot pressure is constant at 45 bar in each step and the variations of the load pressure from nominal pressure (100 bar) should be recorded. These recorded load pressures for each input current are used in flow simulation as boundary conditions.

In Figure 19, the experimental data and the simulated curve are compared according to four following principal variables:

- **Flow gain:** Flow gain is the slope of the linear zone of the flow-current curve. This zone is one of the most important characteristics of a flow control valve. In Figure 20, the calculated flow gain from the experimental and simulated data are compared. According to this figure, experimental gain is 0.355 and simulated gain is 0.352 (0.85% error).
- **Saturation flow:** According to Figure 19, it can be said that the experimental and simulated data show the flow saturation to happen at about 5 Lit/Min.
- **Saturation current:** The saturation current is corresponding current of the saturation flow. According to Figure 19, it can be said that for both of them, the flow is saturated at about 20 mA.
- **Dead zone:** Dead zone is due to the lapping of



Table 1. Experimental and simulation results.

	Flow Gain (lit/Min.mA)	Saturation Flow (lit/mA)	Saturation Current (mA)	Dead Zone (mA)
Experiment	0.355	5	20	0
Simulation	0.352	5	20	1
Error	0.85%	0	0	1

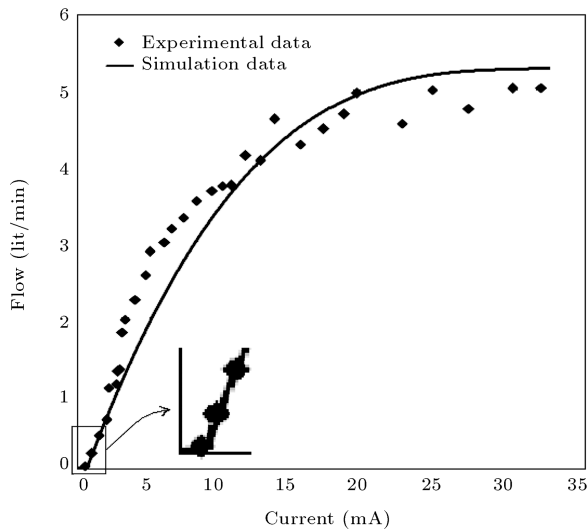


Figure 19. Simulated results versus the experimental data for the flow-current curve in steady state conditions.

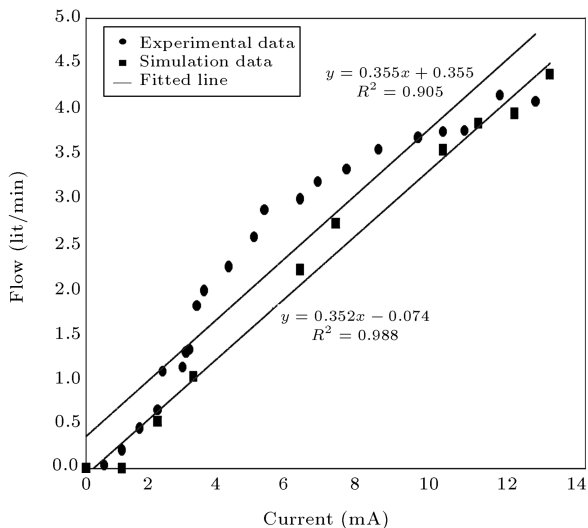


Figure 20. Simulated and experimental flow gain.

the spool and the ports. Since the lapping of this sample valve is measured to be about +0.01 mm, it is expected that a dead zone exists in the flow-current curve. This zone in the simulated curve is seen to be up to 1 mA. However, it is not seen in the experimental results. As the lapping of the spool and the port is very critical, sensing of this

zone in the flow-current test requires more accurate equipment.

### Source of Errors

As the flow-current curve is the final stage in the simulation of the valve behavior, it can be said that all errors of the previous stages appear in this stage too. Also some simplifications such as neglecting the pressure drop in the filters and pipes contributed to the error. However, it seems that neglecting the friction between the cylinder and the piston of the jack and the piston inertia may be the most important sources of error.

### CONCLUSION

In this work, the flow-current characteristic of a sample electro-hydraulic servo valve was simulated. Also a hydraulic tester was constructed to test some behaviors of the valve experimentally. The model incorporates all components of the valve (first and second stage). The experimental and simulation results were compared for four important variables in Table 1. According to Table 1, the valve has a sufficient accuracy. As a result, the model can be used for other studies such as sensitivity analysis. Using this approach, modeling of underlapped, critical center (zerolapped) and overlapped valves can be done in similar studies.

### ACKNOWLEDGMENT

The authors would like to express thanks to M. Gheisari for his helps in torque motor modeling, and M. Hemmati for his helps in the CFD analysis. Thanks to M. Karimi and H. Farajian Zade for their various helps. The experiments are supported financially by Moje-Pouya Inc.

### NOMENCLATURE

- $E$  electrical potential
- $N$  turns of coil
- $i$  electrical current
- $R_{i(i=1,2,3,4)}$  reluctance

$\phi$	magnetic flux
$k$	equilibrium distance of armature and body (equilibrium gap)
$x$	displacement of the armature end
$\mu_0$	magnetic permeability of air
$\mu_r$	relative magnetic permeability of the substance
$A$	area normal to the flux path in the air gap
$B$	magnetic flux density
$w$	electromagnetic energy
$f$	armature force
$T_t$	the produced torque by torque motor
$T_s$	resistance torque of the flexure tube
$F$	pilot fluid force
$r$	radius of the flapper from pivot to pilot fluid forces
$J$	polar mass moment of inertia of the flapper and armature
$c$	damping coefficient of armature and flapper
$\theta_f$	rotation angle of the flapper
$x_f$	flapper displacement
$K_s$	stiffness of the flexure tube
$L_a$	Arm length of the armature
$L$	equilibrium distance between the nozzle and the flapper ( $L = 0.06$ mm)
$\Delta p$	pressure difference
$P_o$	port opening
$S_d$	spool displacement
$l_p$	lapping of the spool and the port

## REFERENCES

1. Tawfic, M.N. "Model based control of an electro-hydraulic servo valve", PhD Thesis, University of Akron, Akron-Ohio, US (1999).
2. Eryilmaz, B. and Wilson, B.H. "Unified modeling and analysis of a proportional valve", *J. Franklin Institute*, **343**, pp. 48-68 (2000).
3. Johnson, J.L. "So what is the difference between a proportional valve and a servo valve", *J. Hydraulics & Pneumatics*, **55**(9), pp. 24-26 (2002).
4. Merritt, H.E., *Hydraulic Control Systems*, John Wiley and Sons, New York, US (1967).
5. Mookherjee, S. "Design and sensitivity analysis of a single-stage electro-hydraulic servo valve", *Proc. of 1st FPNI-PhD Symp.*, Hamburg, Germany, pp. 71-88 (2000).

6. Kim, D.H. and Tsao, T.C. "A linearized electro-hydraulic servo valve model for valve dynamics sensitivity analysis and control system", *J. ASME DSC*, **122**, pp. 179-187 (2000).
7. Noah, D.M., *Hydraulic Control Systems*, John Wiley and Sons, New York, US (2005).
8. Amirante, R. et al. "Evaluation of the flow forces on an open center-directional control valve by means of a computational fluid dynamic analysis", *J. Energy Conversion and Management*, **47**, pp. 1748-1760 (2006).
9. Del Vescovo, G. and Lippolis, A. "CFD analysis of flow forces on spool valves", *1st Int. Conf. on Computational Methods in Fluid Power Technology*, Melbourne, Australia (2003).
10. Cheng, D.K., *Field and Wave Electromagnetics*, 2nd Ed., Addison-Wesley, Massachusetts, US (1989).
11. Walters, R.B., *Hydraulic and Electro-Hydraulic Control Systems*, ELSEVIER Science Publisher LTD (1991).

## BIOGRAPHIES

**Mohammad Saleh Sadooghi** received his B.S. degree from Sharif University of Technology in Tehran, I.R. Iran and his M.S. degree from Bu-Ali Sina University in Hamedan, I.R. Iran, in Applied Mechanics, in 2008. He is now a teacher of robotics engineering at Hamedan University of Technology. His favorite research is Modeling of Electro-Hydraulic Systems as well as Robotic Systems in Vehicles.

**Rahman Seifi** received his Ph.D. degree in Mechanical Engineering in 2004 from the University of Tarbiat Modarres, Tehran, I.R. Iran. He is now a faculty member of mechanical engineering at Bu-Ali Sina University in Hamedan where he teaches courses at the 'Applied Design group' of the Mechanical Engineering Department. His teaching focuses on Automatic Control, Strength of Material, Fracture Mechanics at undergraduate and graduate levels. Dr Seifi has also published 6 articles in international journals and about 50 conference papers.

**Mahmoud Saadat Foumani** received his Ph.D. degree in Mechanical Engineering from Sharif University of Technology, Tehran, I.R. Iran, in 2002. He was a Faculty member at Semnan University from 2002 to 2006 and is now a faculty member of Sharif University of Technology, Mechanical Engineering Department. He teaches courses at the 'Applied Design group' at undergraduate and graduate levels. His teaching focuses on Mechanical Engineering Design, Vehicle Dynamics and Chassis Design and Advanced Mathematics.